Millimeter-Wave Channel Measurements at 28 GHz in Digital Fabrication Facilities

Dmitrii Solomitckii
Tampere University
Tampere, Finland
dmitrii.solomitckii@tuni.fi

Markus Allén
Tampere University
Tampere, Finland
markus.allen@tuni.fi

Davit Yolchyan
National Instruments
Yerevan, Armenia
davit.yolchyan@ni.com

Hrayr Hovsepyan
National Instruments
Yerevan, Armenia
hrayr.hovsepyan@ni.com

Mikko Valkama
Tampere University
Tampere, Finland
mikko.valkama@tuni.fi

Yevgeni Koucheryavy
Tampere University
Tampere, Finland
evgeny.kucheryavy@tuni.fi

***Abstract*—The unprecedented amount of bandwidth available at the millimeter-wave band brings new opportunities for the next-generation factory automation. By supporting these frequencies, the communication technologies may significantly improve the safety and efficiency of manufacturing processes. This paper presents channel measurement results at 28 GHz in a factory environment. The primary channel properties such as path loss, delay, and angular spread are evaluated. Additionally, the distribution of the cross-polarization ratio is shown.**

***Index Terms*—5G systems, factory automation, millimeter-wave communication, channel measurement, radio channel properties**

I. Introduction

The success of the so-called Industry 4.0/5.0 is speculative without the introduction of new wireless technologies, enabling to connect heterogeneous sensors/devices/machines into a single industrial network. Realization of such ambitious plans complies with the emerging fifth generation (5G) wireless technologies, which combine two essential concepts, namely machine-type communications (MTC) and industrial Internet of Things (IoT) [1]. These concepts are intended to meet the perspective demands in network scalability, reliability and latency [2].

At the same time, the millimeter-wave (mmWave) spectrum above 20 GHz is proposed for the 5G wireless technologies to overcome the traditional scarcity of the RF spectrum and deliver unprecedented data rate for performance-hungry applications. Recent publications, such as [3]–[7] and the references therein, describe several mmWave channel measurements performed in various indoor and outdoor scenarios. However, the understanding of mmWave channel properties in factory environments is still minimal. As compared to other indoor areas, the industrial environments tend to include a broad variety of moving and stationary metal equipment, machinery, robots as well as other surfaces that strongly affect radio signal propagation behavior.

The ray-tracing characterization of mmWave channel properties in factory automation deployment was accomplished earlier in [8], but actual radio channel measurements were not performed. Hereat, we continue the investigation of signal propagation in factory environment by carrying out 28 GHz channel sounding. Additionally, power-, angle- and time-related channel properties, as well as depolarization effects are evaluated.

This paper is organized as follows. Section II introduces basic formulas employed in the paper. Then Section III describes our channel sounding equipment operating at 28 GHz. Scenario and procedure of the measurements are defined in Section IV while the results are analyzed in Section V. The final Section VI concludes the paper.

II. Wireless Channel Characterization

A signal radiating from a transmitter (Tx) reaches a receiver (Rx) via many paths. In case of omnidirectional Tx and directive Rx this phenomenon can be described with the *directional channel impulse response* (CIR) as next:

$$h(\tau, \Omega^{\mathrm{Rx}}) = \sum_{n=1}^{N} a_n e^{-j\phi_n} \delta(\tau - \tau_n) \delta(\Omega^{\mathrm{Rx}} - \Omega_n^{\mathrm{Rx}}), \quad (1)$$

where a_n denotes the complex amplitude, τ_n is propagation delay, $\Omega_n^{\mathrm{Rx}} = [\phi_n^{\mathrm{Rx}} \ \theta_n^{\mathrm{Rx}}]$ is angle of arrival (AoA) of n^{th} multipath component (MPC). The total number of the MPCs arriving to the Rx is N. The algorithm shown in [9] might be employed to convert the directional CIR $h(\tau, \Omega^{\mathrm{Rx}})$ into omnidirectional one $h(\tau)$.

To filter out small-scale fading, the CIRs are converted to a power delay profile (PDP) as next:

$$PDP(\tau, \Omega^{\mathrm{Rx}}) = \frac{1}{M} \sum_{m=1}^{M} |h(\tau, \Omega^{\mathrm{Rx}})|^2, \quad (2)$$

where M = 32 is the number of CIRs participating in the time averaging procedure. Additionally, integration of the PDP over time results to total received power. Thus, power angular profile (PAP) specifies the total received power as a function

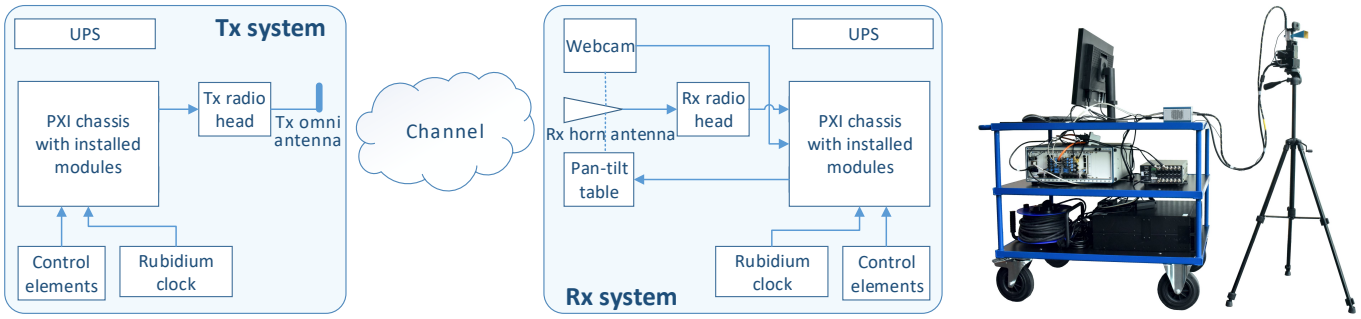

(a) (b)

Fig. 1. (a) Block diagram of the complete millimeter-wave measurement setup: Tx system and Rx system are located in their own movable carts. No cables are required between the carts during the channel measurements. (b) Photograph of Rx system: The tripod holds a horn antenna, a webcam and a computer-controlled pan/tilt unit. The rest of the Rx system has been installed in the cart.

of AoA. Finally, the difference between the total received and transmit powers derives the pathloss (PL).

The root-mean-square (RMS) delay spread (DS), describing the delay dispersion, is specified as follows:

$$\tau_{\mathrm{RMS}} = \sqrt{\frac{\int_{-\infty}^{\infty} PDP(\tau)\tau^2 \mathrm{d}\tau}{\int_{-\infty}^{\infty} PDP(\tau)\mathrm{d}\tau} - \tau_{\mathrm{m}}}, \tag{3}$$

where τ_{m} is the mean delay. Additionally, in the scope of this paper, we utilize the RMS azimuth (ϕ) spread (AS), which is specified as next:

$$S_{\mathrm{RMS}} = \sqrt{\frac{\int |e^{j\phi} - \mu_\phi|^2 PAS(\phi)\mathrm{d}\phi}{\int PAS(\phi)\mathrm{d}\phi}}, \tag{4}$$

where μ_ϕ is the mean angular value and $PAS(\phi)$ refers to power angular spectrum.

The polarization of the transmitting signal may change due to interaction with surrounding objects, contributing both orthogonal polarization branches on Rx. The difference between these branches is determined by cross-polarization ratio (XPR) as follows:

$$XPR = 20\log_{10}(|E^{\mathrm{co}}|/|E^{\mathrm{x}}|), \tag{5}$$

where E^{co} and E^{x} are co- and cross-polarized signal arriving to Rx.

III. Measurement Setup

The core part of our measurement setup comprises the NI mmWave equipment, which is described in Section III-A. We have complemented the setup by additional units to expand its capability and meet the requirements of the mmWave channel measurements. The details are given in Section III-B.

A. The NI mmWave Equipment

The NI mmWave equipment is documented in detail in [10] and the references therein. It has a modular structure, and the exact hardware configuration depends on required capabilities: RF frequency range, uni- or bidirectional, SISO or MIMO. A PXI chassis houses all the necessary modules. In our setup, we have two PXIe-1085 chassis, one for Tx side and one for Rx side. Both chassis include the modules listed in Table I. The first slot has PXIe-8880, which is basically a computer running Windows 7 operating system. It is used for controlling and configuring all the other modules in the chassis using the LabVIEW programming environment.

The PXI chassis modules together are able to generate an arbitrary waveform with an instantaneous bandwidth of 2 GHz. The PXI chassis provides the waveform at intermediate frequency (IF), which can be selected between 8.5 GHz and 13 GHz. The IF waveform and LO signal (supplied by PXIe-3620) are fed into an external Tx radio head. In our setup, the Tx radio head is mmRH-3642, which supports RF frequency range of 24.25–33.40 GHz. On the Rx side, the external radio head is mmRH-3652, which supports the same aforementioned RF frequency range, while the instantaneous Rx bandwidth is 2 GHz. The Rx radio head provides the received IF signal, which then fed into another PXI chassis with similar modules as the first one.

B. Advanced Measurement Setup

Our measurement setup is mobile, and it does not require any cables between Tx and Rx sides during the measurements. Mobility is achieved by building the setup on two carts; one

TABLE I
NI PXIe-1085 Chassis Content

Slot #	Device	Description
1	PXIe-8880	Embedded controller
3	PXIe-7902	High-speed serial FPGA module
4	PXIe-7902	High-speed serial FPGA module
5	PXIe-3610	I/Q generator
6–7	PXIe-3620	RF upconverter/downconverter module
8	PXIe-3630	I/Q digitizer
9	PXIe-7902	High-speed serial FPGA module
10	PXIe-6674T	Timing module
12	PXIe-7902	High-speed serial FPGA module

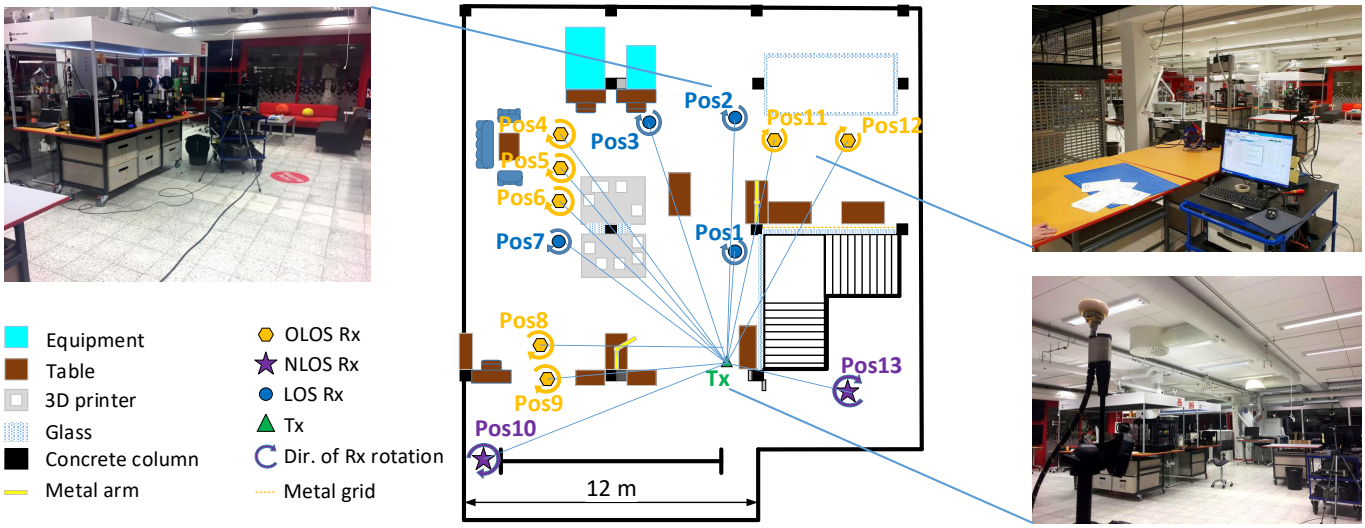

Fig. 2. Millimeter-wave channel measurements are carried out in digital fabrication facilities of Fablab Tampere.

cart for Tx equipment and another one for Rx equipment. The overall setup is illustrated in the block diagram of Fig. 1a. A photograph of a fully equipped cart is shown in Fig. 1b.

The NI mmWave equipment consists of PXI chassis and radio head. To maintain proper synchronization between Tx and Rx side, we have a rubidium clock on both sides. The exact device model is Standford Research Systems FS725. It provides 10 MHz and 1 PPS signals, which are fed into the PXIe-6674T located in the PXI chassis. During the calibration phase, the two rubidium clocks are synchronized using 1 PPS signal. After synchronization, the cable between the clocks can be detached. The mobility of the system is further enhanced by having uninterruptible power supplies (UPS) in the carts. We have an Eaton 5PX 2200iRT UPS with an extended battery module (5PXEBM48RT) in both carts, which means that we can run the system over one hour with the batteries.

We installed additional antennas on the radio heads. On Tx side, we use SAGE Millimeter SAO-2734030345-KF-S1 omnidirectional antenna with 3 dBi gain for the frequency range of 26.5–40 GHz. On Rx side, we have Pasternack PE9851A-20 horn antenna with a nominal gain of 20 dBi for the frequency range of 22–33 GHz. To perform efficient exploitation of the directive antenna, a control unit for fine-rotation is utilized. We have attached the antenna to a FLIR PTU-E46-17 pan/tilt unit using a custom-made aluminum holder. The pan/tilt unit is able to provide a fraction of a degree accuracy for antenna rotation, and it is controlled from the PXIe-8880 computer. Moreover, we have attached a Logitech HD Webcam B525 on top of the horn antenna, so that we can also capture visual images from the Rx point of view. The complete antenna system sits on a tripod introducing versatility of the measurement setup.

We have also added Wi-Fi connection (IEEE 802.11ac) between the Tx and Rx PXI chassis for remote control and data exchange between the carts. This is implemented using Zyxel NWD6605 USB 3.0 dongles. It should be noted that the wireless data connection does not interfere with our channel measurements, because Wi-Fi uses significantly lower frequencies than 28 GHz. User interaction with the overall measurement setup is enabled using regular control elements, namely a keyboard, a mouse and a monitor.

IV. Deployment and Procedure of Measurement

Wireless channel sounding is carried out in the Fablab Tampere, which is an open learning environment established in Tampere University in Finland as a part of the global concept developed in the Massachusetts Institute of Technology (MIT). The primary goal of the Fablab Tampere is to provide digital fabrication facilities for staff and students of Tampere University.

The channel sounding takes place in the manufacturing zone having the area of 13 m^2 shown in Fig. 2, where items and materials are illustrated with different colors and symbols. The manufacturing machines (gray and cyan) include 3D printers, laser cutters, and other equipment. The furniture (brown and blue) refers to tables, chairs, and couches. The mechanical parts such as metallic arms and separating grid are illustrated with yellow. The building units (black) include walls, pillars, stairs, etc.

The measurements are executed in 13 Rx positions, while the Tx location is fixed. All the measurements are divided into the line of sight (LOS), obstructed LOS (OLOS) and non-LOS (NLOS). More detailed information about each of the 13 measuring conditions is listed in Table II. Even in case of LOS visibility between omnidirectional Tx and directive Rx, third-party objects may fall into the Fresnel zone causing interference.

The measurement procedure starts with placing the Rx antenna on the height of 1.6 m in one of the 13 positions. Next, by using a laser distance meter, beam alignment of the Rx with respect to Tx is accomplished in LOS and OLOS conditions. For the NLOS case, the alignment of the Rx is made using relative geometric measurements.

TABLE II
CHANNEL MEASUREMENT CONDITIONS

Pos #	Visibility	Conditions
1	LOS (3.8 m)	Reflection from surrounding objects
2	LOS (8.3 m)	Reflection from surrounding objects and ground
3	LOS (8.6 m)	Reflection from table
4	OLOS (9.1 m)	Obstructed by 3D printers and glass cabinet
5	OLOS (9.2 m)	Obstructed by 3D printers and a column
6	OLOS (9.2 m)	Obstructed by glass cabinet
7	OLOS (8.3 m)	LOS, but lots of 3D printers in Fresnel zone
8	OLOS (7.0 m)	Obstructed by metal arm
9	OLOS (9.0 m)	Obstructed by concrete column
10	NLOS (10 m)	Obstructed by wooden wall and metal lockers
11	OLOS (9.0 m)	Obstructed by metal arm
12	OLOS (9.8 m)	Partially obstructed by metal grid
13	NLOS (10 m)	Obstructed by stairs and concrete column

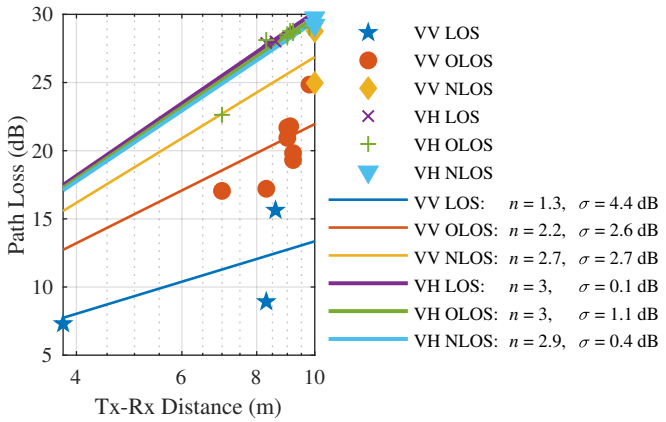

Fig. 3. Omnidirectional path loss.

After the Rx beam alignment, the Rx antenna is rotated to the initial AoA position of −150° to a theoretical straight line between the Tx and Rx (the dashed blue lines in Fig. 2). During the measurement, the Rx scans the azimuth AoA range of −150°...150° passing through the direction of Tx on 0°. The scanning step is 5°, which corresponds to 30 CIR measurements per position. The elevation angle ($\theta = 0°$) is not changed during the measurements.

Each Rx position is measured using co-polarized vertical (V) and cross-polarized horizontal (H) orientation of the Rx relative to the vertically polarized Tx to estimate the effect of depolarization. The change of polarization type is implemented by rotating the Rx antenna by 90° around its polarization plane (perpendicular to the direction propagation).

V. CHANNEL MEASUREMENT RESULTS

A. Path Loss

In order to obtain omnidirectional PL, the algorithm proposed in [9] is applied, which sums up incoherently all the signals coming from different AoAs excluding any antenna gains. Obtained omnidirectional PL is shown in Fig. 3. Additionally, each of the data sets is approximated by single-slope *Close-in Free Space Reference Distance Model* [9] specified by n and σ coefficients. Particularly, $n \approx 3$ for VH case, but varies from 1.3 to 2.7 for VV condition. The results correlate with those obtained in [3] at 28 GHz for the indoor deployment. The standard deviation σ varies from 2.6 dB to 3.1 dB for VV and is maximum of 1.1 dB for VH conditions.

TABLE III
OMNIDIRECT. RMS DELAY SPREADS AND RMS ANGULAR SPREADS

Pos #	Delay Spread (ns) VV	Delay Spread (ns) VH	Angular Spread (°) VV	Angular Spread (°) VH
1	38.5	18.1	24.0	69.9
2	37.7	16.7	34.7	59.7
3	10.0	15.0	30.3	64.5
4	18.3	7.1	80.8	70.8
5	12.3	13.0	68.3	75.9
6	12.3	16.3	80.1	93.0
7	12.6	13.3	22.3	45.6
8	16.4	14.6	42.5	41.7
9	12.0	5.7	44.7	54.5
10	22.7	4.0	70.1	89.3
11	21.9	15.1	55.9	85.4
12	20.8	12.4	54.0	56.8
13	19.8	13.5	43.2	43.3
μ	19.6	12.6	50	65
σ	9.2	7.3	20	17

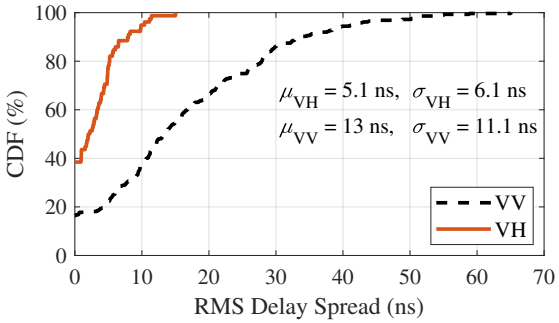

Fig. 4. The CDF of the RMS delay spread for the directive Rx.

B. Delay Spread and Angular Spread

The next investigated channel property is RMS DS obtained for both omnidirectional and directional cases. The directional RMS DS specified by Rx position and AoA are aggregated in cumulative distribution function (CDF) shown in Fig. 4. According to the obtained results, the mean value of the directional RMS DS for the VV case is 2.5 times higher than the mean value for the VH conditions.

Similar behavior can be observed for the omnidirectional RMS DS and RMS angular spread (AS) listed in Table III, where the VH case has smaller values than the VV. However, the mean values of the omnidirectional RMS DS are higher than the directional ones in Fig. 4. This is stemming from factory conditions consisting of a considerable number of distributed machines, which contribute to MPC propagation and increase the spread of the channel properties.

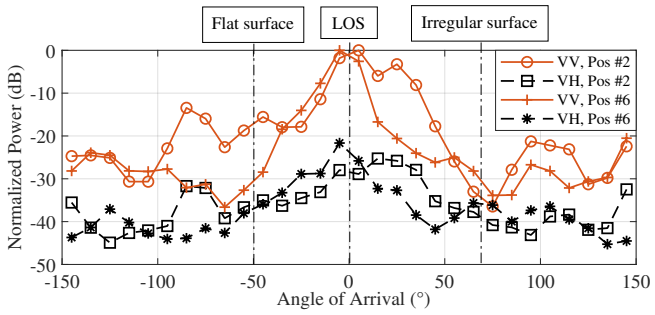

(a)

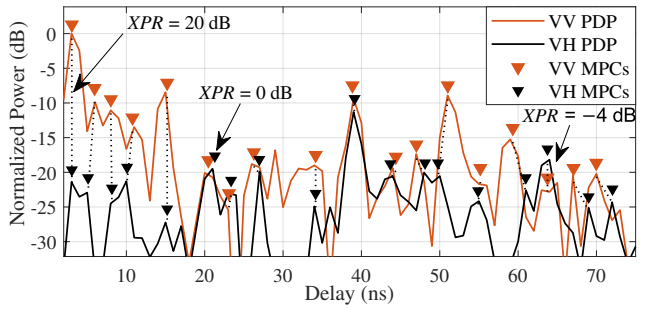

(b)

Fig. 5. (a) Comparison of total received power in VV and VH cases. (b) Power delay profile for 2nd Rx position when AoA is 60°.

C. Cross-Polarization Ratio

First, a preliminary XPR evaluation is completed as a ratio of VV and VH total received power in each of 13 positions and AoAs. As a representative example, two of those 13 data sets (2nd and 6th pos.) represented by PAP are shown in Fig. 5a. Apparently, the XPR in LOS condition (AoA of 0°) is about 20 dB, while AoA of 74° delivers only XPR of 3 dB. Additionally, it is observed that signals reflecting from flat surfaces (AoA = 50°, flat panel on the stairs) produce XPR comparable with LOS, while interaction with complex irregular surfaces (AoA = 70°...80°, 3D printers) significantly reduces the XPR. This suggests that propagation mechanisms affect XPR and should be investigated more accurately at the scale of MPC. Thus, the XPR of an individual PDP is considered. Fig. 5b illustrates the example of PDP on 2nd Rx position, when AoA is 60°. The red peaks in Fig. 5b specify the powers of the VV MPCs, while the black profile shows the VH MPCs. The XPR values are obtained with the house-built searching algorithm that compares the adjacent correlated peaks with each other (see the dashed black lines in Fig. 5b).

Finally, the XPRs specified by the total received power and PDP are aggregated in CDF in Fig. 6, which includes all the data from the 13 Rx positions. It is obvious that the total received power XPRs are more than 0 dB for all cases, and only 40 % of those are less than 10 dB. Apparently, about 15 % of all MPCs have XPR less than 0 dB and 40 % of them below than 5 dB.

VI. Conclusion

In this paper, an analysis of channel characteristics in the factory environment was carried out using wideband channel sounding equipment at 28 GHz. Path loss, delay, and angular spreads, as well as XPR were studied. Specifically, the PL coefficient n varied from 1.3 to 2.7 for VV and was about 3 for the VH condition. The mean RMS DS was 14 ns for VV and 4 ns for VH cases. Finally, it was demonstrated that some of the MPCs may contribute 15 % of negative XPRs due to interaction with complex and irregular objects.

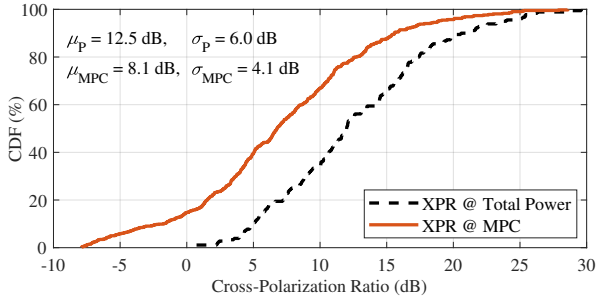

Fig. 6. CDFs of obtained cross-polarization ratios.

References

[1] J. Sachs, G. Wikström, T. Dudda, R. Baldemair, and K. Kittichokechai, "5G radio network design for ultra-reliable low-latency communication," *IEEE Netw.*, vol. 32, no. 2, pp. 24–31, Mar./Apr. 2018.

[2] O. N. C. Yilmaz, Y.-P. E. Wang, N. A. Johansson, N. Brahmi, S. A. Ashraf, and J. Sachs, "Analysis of ultra-reliable and low-latency 5G communication for a factory automation use case," in *Proc. 2015 IEEE Int. Conf. Communication Workshop (ICCW)*, London, UK, Jun. 2015, pp. 1190–1195.

[3] S. Deng, M. K. Samimi, and T. S. Rappaport, "28 GHz and 73 GHz millimeter-wave indoor propagation measurements and path loss models," in *Proc. 2015 IEEE Int. Conf. Communication Workshop (ICCW)*, London, UK, Jun. 2015, pp. 1244–1250.

[4] T. S. Rappaport, F. Gutierrez, E. Ben-Dor, J. N. Murdock, Y. Qiao, and J. I. Tamir, "Broadband millimeter-wave propagation measurements and models using adaptive-beam antennas for outdoor urban cellular communications," *IEEE Trans. Antennas Propag.*, vol. 61, no. 4, pp. 1850–1859, Apr. 2013.

[5] Y. Azar, G. N. Wong, K. Wang, R. Mayzus, J. K. Schulz, H. Zhao, F. Gutierrez Jr., D. Hwang, and T. S. Rappaport, "28 GHz propagation measurements for outdoor cellular communications using steerable beam antennas in New York city." in *Proc. 2013 IEEE Int. Conf. Communications (ICC)*, Budapest, Hungary, Jun. 2013, pp. 5143–5147.

[6] X. Wu, Y. Zhang, C.-X. Wang, G. Goussetis, e.-H. M. Aggoune, and M. M. Alwakeel, "28 GHz indoor channel measurements and modelling in laboratory environment using directional antennas," in *Proc. 2015 9th European Conf. Antennas and Propagation (EuCAP)*, Lisbon, Portugal, Apr. 2015, pp. 1–5.

[7] X. Yin, C. Ling, and M.-D. Kim, "Experimental multipath-cluster characteristics of 28-GHz propagation channel," *IEEE Access*, vol. 3, pp. 3138–3150, 2015.

[8] D. Solomitckii, A. Orsino, S. Andreev, Y. Koucheryavy, and M. Valkama, "Characterization of mmwave channel properties at 28 and 60 GHz in factory automation deployments," in *Proc. 2018 IEEE Wireless Communications and Networking Conf. (WCNC)*, Barcelona, Spain, Apr. 2018, pp. 1–6.

[9] S. Sun, G. R. MacCartney Jr., M. K. Samimi, and T. S. Rappaport, "Synthesizing omnidirectional antenna patterns, received power and path loss from directional antennas for 5G millimeter-wave communications," in *Proc. 2015 IEEE Global Communications Conf. (GLOBECOM)*, San Diego, CA, Dec. 2015, pp. 1–7.

[10] National Instruments. Introduction to the NI mmWave transceiver system hardware. [Online]. Available: http://www.ni.com/product-documentation/53095/en/